Electronic Supplementary Material and Guide

	Supplemental methods
Figure S1	Marker implantation sites for Indiv1 (Cat 01)
Table S1	Markers implanted in Indiv1 (Cat 01)
Figure S2	Marker implantation sites for Indiv2 (Cat 02)
Table S2	Markers implanted in Indiv2 (Cat 02)
Figure S3	Marker implantation sites for Indiv3 (Cat 05)
Table S3	Markers implanted in Indiv3 (Cat 05)
Movie S1	X-ray video of catfish feeding from a lateral view
Movie S2	X-ray video of catfish feeding from a dorsoventral view
Table S4	Ranges of maximum speed and maximum pressure differential in each bin
Movie S3	Unification of CT markers (and meshes) with X-ray markers
Table S5	Variability in marker-to-marker distances for each body
Movie S4	Video of Indiv1 (Cat 01) eating pellets (not used for data collection)
Movie S5	Video of Indiv2 (Cat 02) eating a worm (not used for data collection)
Figure S4	Intracranial joint model fits for Indiv1 (Cat 01)
Figure S5	Intracranial joint model fits for Indiv2 (Cat 02)
Figure S6	Intracranial joint model fits for Indiv3 (Cat 05)
Figure S7	Principal intracranial rotations for Indiv1 (Cat 01)
Figure S8	Principal intracranial rotations for Indiv2 (Cat 02)
Figure S9	Principal intracranial rotations for Indiv3 (Cat 05)
Figure S10	Intracranial motion pairwise plot for Indiv1 (Cat 01)
Figure S11	Intracranial motion pairwise plot for Indiv2 (Cat 02)
Figure S12	Intracranial motion pairwise plot for Indiv3 (Cat 05)
Figure S13	Motor integration patterns for Indiv1 (Cat 01)
Figure S14	Motor integration patterns for Indiv2 (Cat 02)
Figure S15	Motor integration patterns for Indiv3 (Cat 05)
Figure S16	Mean motion integration differences by task, speed, and pressure differential
Table S6	Table version of Figure 6
Kinematic data	These three files (Kinematic data Indiv1.csv, Kinematic data Indiv2.csv, Kinematic data Indiv3.csv) contain the principal rotations of each skeletal element and associated metadata for each individual. Column names indicate each data category and rows correspond to each frame. Skeletal rotation columns are named by the skeletal element name followed by a number (1 for primary axis rotations, 2 for secondary axis rotations). Time is in seconds. For the "Behavior" column "ingestion" is used synonymously with "capture". Rotations are in radians. Pressure is in kPa. Velocities are in degrees per second. Hypaxial length is in mm

Supplemental methods

In vivo data collection. Due to the high radio-opacity of water we used custom-designed acrylic aquaria ("Tunnel tank") having a narrow extension (from the main portion of the tank) less than 10 cm wide and with a water depth of less than 15 cm (Gidmark et al., 2012). Indiv1 and Indiv3 were filmed while feeding in this extension with the X-ray emitters and image intensifiers (Imaging Systems and Service, Painesville, OH, USA) arranged to provide lateral and dorsoventral perspectives. Indiv2 was filmed from two oblique dorsoventral perspectives in the main portion of the tank. X-rays were generated at 100 mA and 80-120 kVp and X-ray images were recorded with Phantom v10 high-speed cameras (Vision Research, Wayne, NJ, USA) at 1,760×1,760 pixel resolution, and 300 frames per second with a 1/1000 s shutter speed; at these settings we were limited to a maximum of 10 seconds of recording. We recorded intraoral pressures at 1,000 Hz using an SPR-407 Mikro-tip pressure probe (Millar Instruments) via PowerLab and LabChart 7.2.2 (AD Instruments). For calibration we took images of a perforated metal sheet for distortion correction and of calibration objects (objects with markers in known 3D locations) to reconstruct marker pixel coordinates from each view into 3D coordinates (Knorlein et al., 2016). After all *in vivo* data collection, we sacrificed all experimental animals using MS-222 (at 1 g/L) and scanned each using computed tomography (CT) at 480×480 pixel resolution and 0.22-0.34 mm slice thickness (FIDEX CT Scanner, Animage, LLC; Pleasanton, CA, USA).

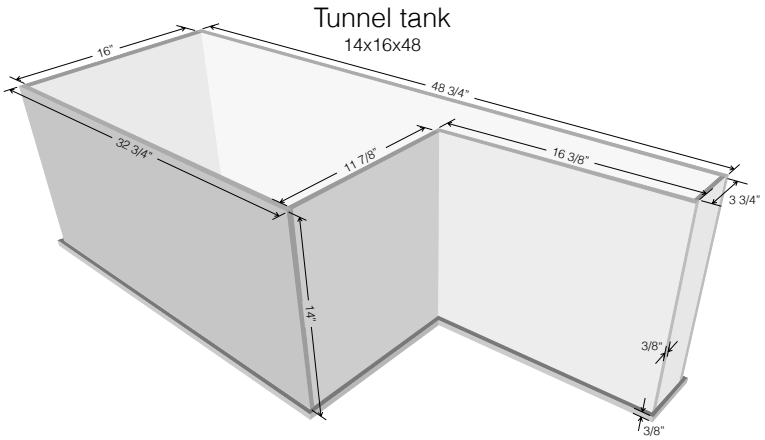

Main portion volume (14" x 16" x 32"):	31 gal (7168 in^3)
Tunnel volume (14" x 3 3/4" x 16"):	3.6 gal (840 in^3)
Total tank volume:	34.6 gal (8008 in^3)

Design by Nick Gidmark
Illustration by Aaron Olsen

XROMM animation. We reduced the vertex counts of each mesh using Meshlab v2016.12 (meshlab.net). The average tracking rate in XMALab was 0.54 sec per frame and per bead. We smoothed marker 3D coordinates using the 'smoothMotion' function (matools R package; github.com/aaronolsen), using adaptive smoothing to apply different span parameters depending on the marker's velocity. For each individual, the CT marker "constellations" for each skeletal element were optimized using the mean of X-ray constellations from a random sample of 100 frames per individual and the 'bestAlign' function (matools); this allows the greater sampling of 3D marker positions from X-ray filming to improve the CT marker positions. Some aspects of our implantation scheme (e.g. skeletal elements with just 2 implanted markers, a nearly collinear set of 3 or more markers) produced unification inaccuracies, evident by skeletal mesh interpenetration (crossing of mesh faces). To account for this, we refined the unifications with two approaches: constraint landmarks and constraint planes. For the constraint landmark approach we identified landmarks where we expect consistent articulation between two joined elements (an already unified element, or "parent", and an element to be unified, or "child"). We

then rotated the child element about a best-fit axis through its markers to minimize deviation from these child-parent constraint landmarks. For the constraint plane approach we defined a plane on the surface of either the child or parent element and points adjoining that plane on the other element. The child element was then rotated (about a best-fit axis through its markers) to eliminate any interpenetrations of the points through the constraint plane. We used constraint landmarks to refine suspensorium, post-temporal, and hyoid unifications and constraint planes to refine pectoral girdle unifications. These approaches allow additional knowledge of the anatomy to reduce uncertainty about the element's pose. The mean unification errors (how well the optimized CT markers aligned with the X-ray markers and also a measure of precision) across all frames and individuals were (mean ± SD): left operculum, 62 μm ± 29 μm; neurocranium, 58 μm ± 18 μm; left post-temporal, 62 μm ± 71 μm; left suspensorium, 106 μm ± 46 μm; left hyoid, 145 μm ± 103 μm; left lower jaw, 92 μm ± 73 μm; left pectoral girdle, 154 μm ± 85 μm. Mean unification error did not exceed 0.15 mm for any skeletal element; this represents a maximum unification error of 0.25% relative to mean individual head length, which ranged from 70 to 81 mm. Hypaxial muscle strain was measured using the distance between the most rostral and the second or third most rostral hypaxial markers using fluoromicrometry (Camp et al., 2016).

Calculating cross-correlation using 'ccfDis'. We calculated the cross-correlation using a modified version of the 'ccf' function, 'ccfDis' (matools R package). The 'ccf' function is intended for two continuous times series. However, by concatenating multiple "sets" (here, trials or events) into a single series we created discontinuous times series. If we were to use 'ccf', the sliding of one signal by different lags relative to the other signal would cause portions from one set to be compared against portions of a different set, which may be at a different phase in the feeding cycle. This would artificially decrease the cross-correlation at greater lags. To correct this we created a 'ccfDis' function for two discontinuous time series. The 'ccfDis' function inserts "buffers" (of NA values) between different sets so that when one signal is slid relative to the other, the edge of one set does not overlap with the edge of a different set. Because these set overlaps would ordinarily only amount to 1-2% of the total time series 'ccfDis' results did not differ by more than 2% from the results of 'ccf'.

References cited in supplemental methods

Camp AL, Astley HC, Horner AM, Roberts TJ, Brainerd EL. 2016 Fluoromicrometry: a method for measuring muscle length dynamics with biplanar videofluoroscopy. *J. Exp. Zool. Part A.* **325**, 399–408. (doi:10.1002/jez.2031)

Gidmark NJ, Staab KL, Brainerd EL, Hernandez LP. 2012 Flexibility in starting posture drives flexibility in kinematic behavior of the kinethmoid-mediated premaxillary protrusion mechanism in a cyprinid fish, *Cyprinus carpio*. *J Exp Biol* **215**(13), 2262–2272. (doi: 10.1242/jeb.070516)

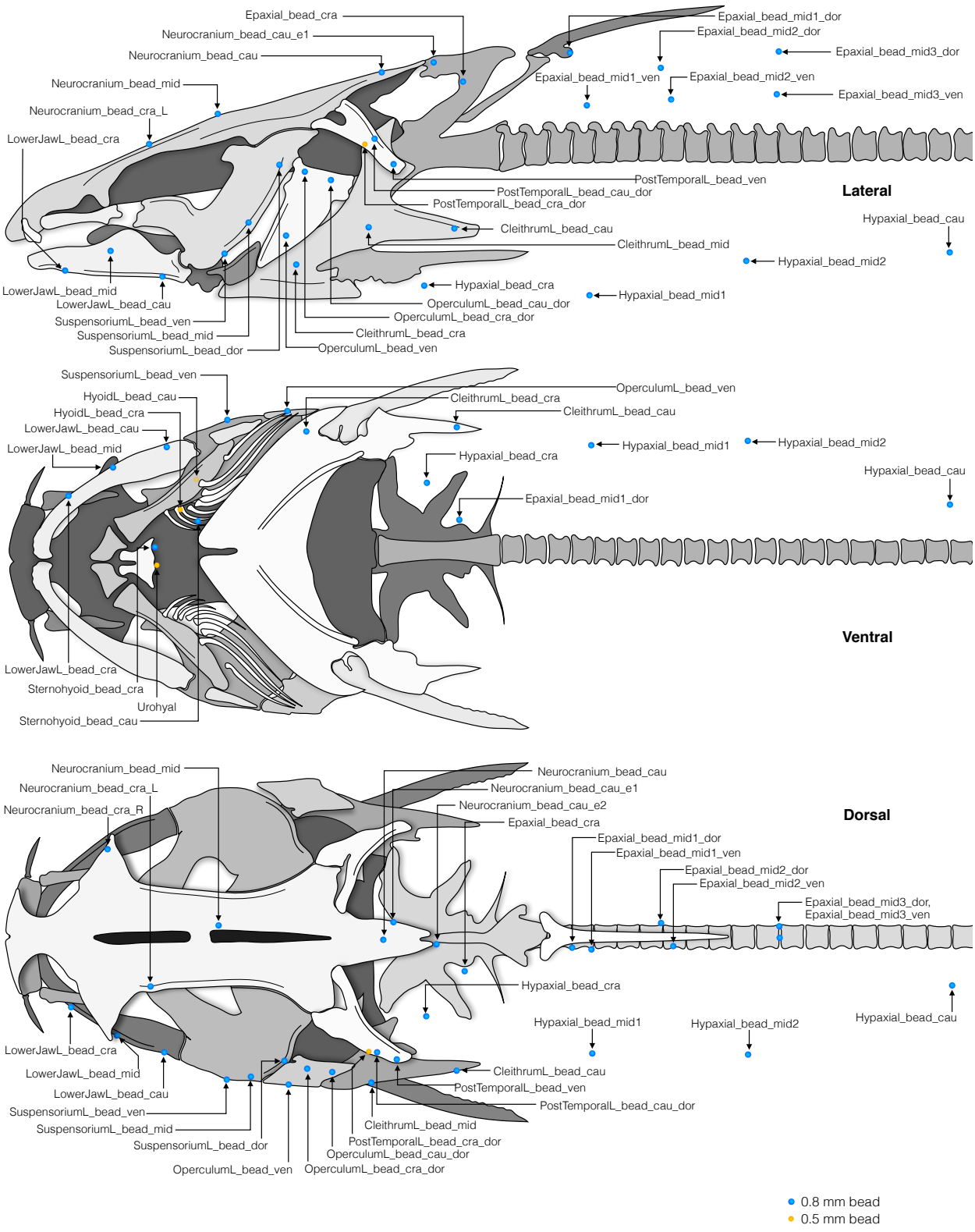

Figure S1. Marker implantation sites for Individual 1 (Cat 01)

Table S1. Markers implanted in Individual 1 (Cat 01)

ID	Name	Bead size (mm)
1	BeadInGut1	NA
2	BeadInGut2	NA
3	BeadInGut3	NA
4	BeadInGut4	NA
5	BeadInGut5	NA
6	CleithrumL_bead_cau	0.8
7	CleithrumL_bead_cra	0.8
8	CleithrumL_bead_mid	0.8
9	Epaxial_bead_cra	0.8
10	Epaxial_bead_mid1_dor	0.8
11	Epaxial_bead_mid1_ven	0.8
12	Epaxial_bead_mid2_dor	0.8
13	Epaxial_bead_mid2_ven	0.8
14	Epaxial_bead_mid3_dor	0.8
15	Epaxial_bead_mid3_ven	0.8
16	HyoidL_bead_cau	0.5
17	HyoidL_bead_cra	0.5
18	Hypaxial_bead_cau	0.8
19	Hypaxial_bead_cra	0.8
20	Hypaxial_bead_mid1	0.8
21	Hypaxial_bead_mid2	0.8
22	LowerJawL_bead_cau	0.8
23	LowerJawL_bead_cra	0.8
24	LowerJawL_bead_mid	0.8
25	Neurocranium_bead_cau	0.8
26	Neurocranium_bead_cau_e1	0.8
27	Neurocranium_bead_cau_e2	0.8
28	Neurocranium_bead_cra_L	0.8
29	Neurocranium_bead_cra_R	0.8
30	Neurocranium_bead_mid	0.8
31	OperculumL_bead_cau_dor	0.8
32	OperculumL_bead_cra_dor	0.8
33	OperculumL_bead_ven	0.8
34	PostTemporalL_bead_cau_dor	0.8
35	PostTemporalL_bead_cra_dor	0.5
36	PostTemporalL_bead_ven	0.8
37	Prey_bead	0.8
38	Sternohyoid_bead_cau	0.8
39	Sternohyoid_bead_cra	NA
40	SuspensoriumL_bead_dor	0.8
41	SuspensoriumL_bead_mid	0.8
42	SuspensoriumL_bead_ven	0.8
43	Urohyal_bead	0.5

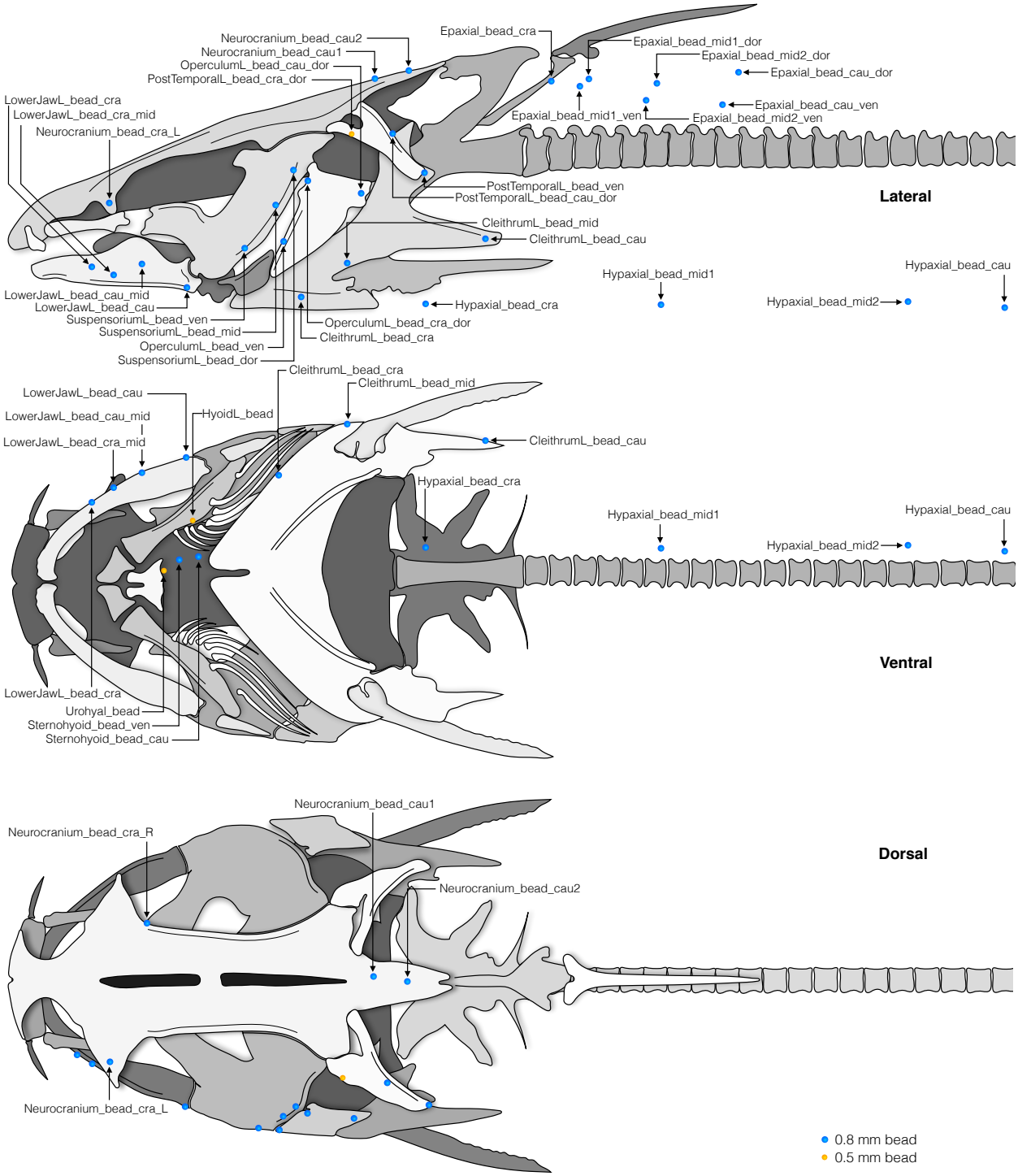

Figure S2. Marker implantation sites for Individual 2 (Cat 02)

Table S2. Markers implanted in Individual 2 (Cat 02)

ID	Name	Bead size (mm)
1	AdditionalBead1	NA
2	AdditionalBead2	NA
3	CleithrumL_bead_cau	0.8
4	CleithrumL_bead_cra	0.8
5	CleithrumL_bead_mid	0.8
6	Epaxial_bead_cau_dor	0.8
7	Epaxial_bead_cau_ven	0.8
8	Epaxial_bead_cra	0.8
9	Epaxial_bead_mid1_dor	0.8
10	Epaxial_bead_mid1_ven	0.8
11	Epaxial_bead_mid2_dor	0.8
12	Epaxial_bead_mid2_ven	0.8
13	HyoidL_bead	0.5
14	Hypaxial_bead_cau	0.8
15	Hypaxial_bead_cra	0.8
16	Hypaxial_bead_mid1	0.8
17	Hypaxial_bead_mid2	0.8
18	LowerJawL_bead_cau	0.8
19	LowerJawL_bead_cau_mid	0.8
20	LowerJawL_bead_cra	0.8
21	LowerJawL_bead_cra_mid	0.8
22	Neurocranium_bead_cau1	0.8
23	Neurocranium_bead_cau2	0.8
24	Neurocranium_bead_cra_L	0.8
25	Neurocranium_bead_cra_R	0.8
26	OperculumL_bead_cau_dor	0.8
27	OperculumL_bead_cra_dor	0.8
28	OperculumL_bead_ven	0.8
29	PostTemporalL_bead_cau_dor	0.8
30	PostTemporalL_bead_cra_dor	0.5
31	PostTemporalL_bead_ven	0.8
32	Prey_bead	0.8
33	Sternohyoid_bead_cau	0.8
34	Sternohyoid_bead_cra	0.8
35	SuspensoriumL_bead_dor	0.8
36	SuspensoriumL_bead_mid	0.8
37	SuspensoriumL_bead_ven	0.8
38	Urohyal_bead	0.5

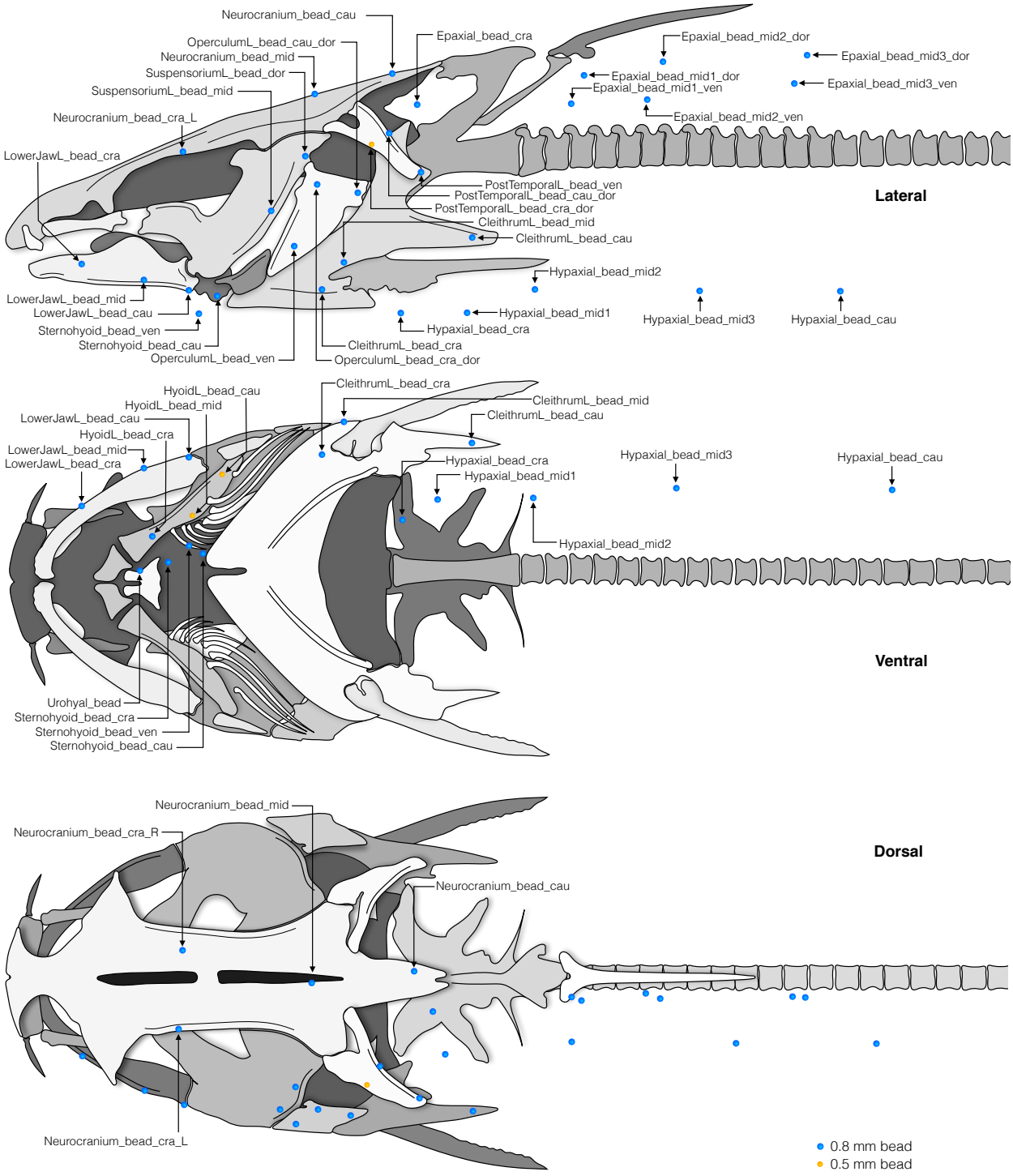

Figure S3. Marker implantation sites for Individual 5 (Cat 05)

Table S3. Markers implanted in Individual 3 (Cat 05)

ID	Name	Bead size (mm)
1	AdditionalBead1	NA
2	AdditionalBead2	NA
3	AdditionalBead3	NA
4	AdditionalBead4	NA
5	CleithrumL_bead_cau	NA
6	CleithrumL_bead_cra	0.8
7	CleithrumL_bead_mid	0.8
8	Epaxial_bead_cra	0.8
9	Epaxial_bead_mid1_dor	0.8
10	Epaxial_bead_mid1_ven	0.8
11	Epaxial_bead_mid2_dor	0.8
12	Epaxial_bead_mid2_ven	0.8
13	Epaxial_bead_mid3_dor	0.8
14	Epaxial_bead_mid3_ven	0.8
15	HyoidL_bead_cau	0.5
16	HyoidL_bead_cra	0.8
17	HyoidL_bead_mid	0.5
18	Hypaxial_bead_cau	0.8
19	Hypaxial_bead_cra	0.8
20	Hypaxial_bead_mid1	0.8
21	Hypaxial_bead_mid2	0.8
22	Hypaxial_bead_mid3	0.8
23	LowerJawL_bead_cau	0.8
24	LowerJawL_bead_cra	0.8
25	LowerJawL_bead_mid	0.8
26	Neurocranium_bead_cau	0.8
27	Neurocranium_bead_cra_L	0.8
28	Neurocranium_bead_cra_R	0.8
29	Neurocranium_bead_mid	0.8
30	OperculumL_bead_cau_dor	0.8
31	OperculumL_bead_cra_dor	0.8
32	OperculumL_bead_ven	0.8
33	PostTemporalL_bead_cau_dor	0.8
34	PostTemporalL_bead_cra_dor	0.5
35	PostTemporalL_bead_ven	0.8
36	Prey_bead	0.8
37	Sternohyoid_bead_cau	0.8
38	Sternohyoid_bead_cra	0.8
39	Sternohyoid_bead_ven	0.8
40	SuspensoriumL_bead_dor	0.8
41	SuspensoriumL_bead_mid	0.8
42	Urohyal_bead	0.8

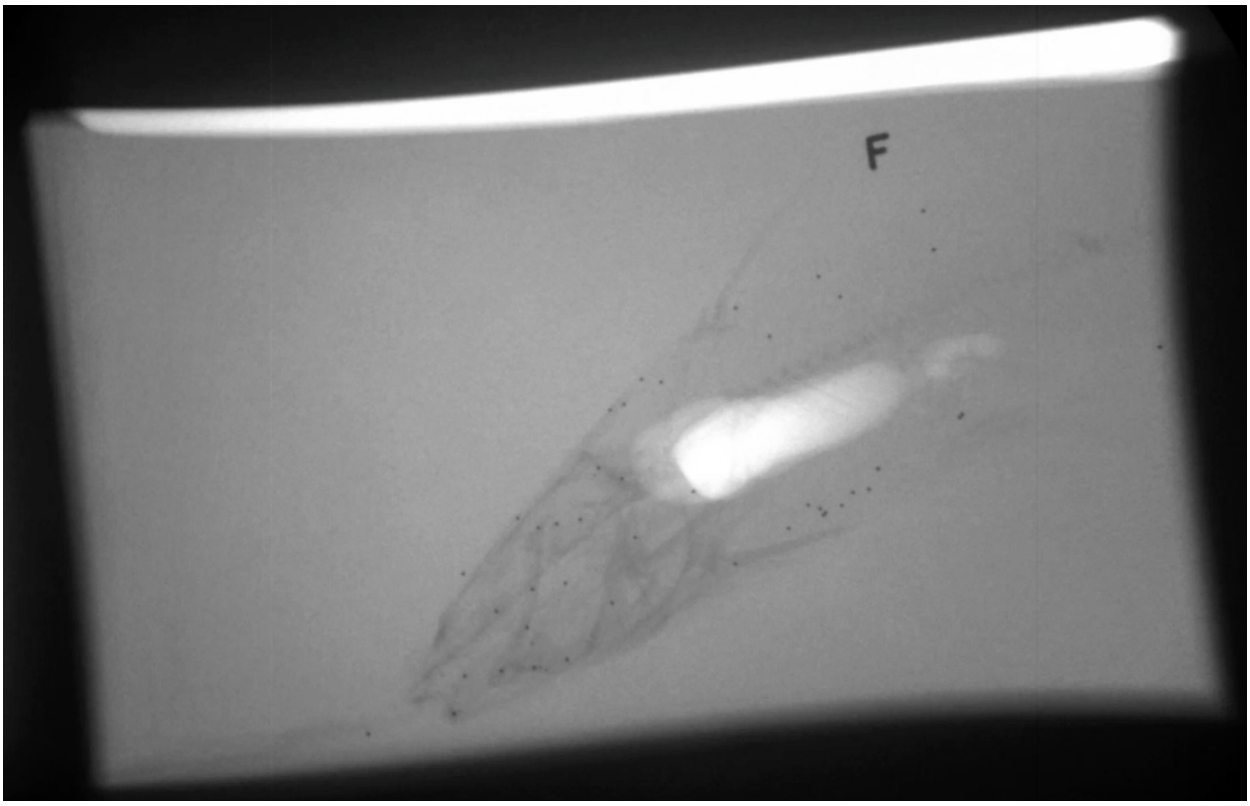

Movie S1. X-ray video of catfish feeding from a lateral view. See supplemental information page for link to video.

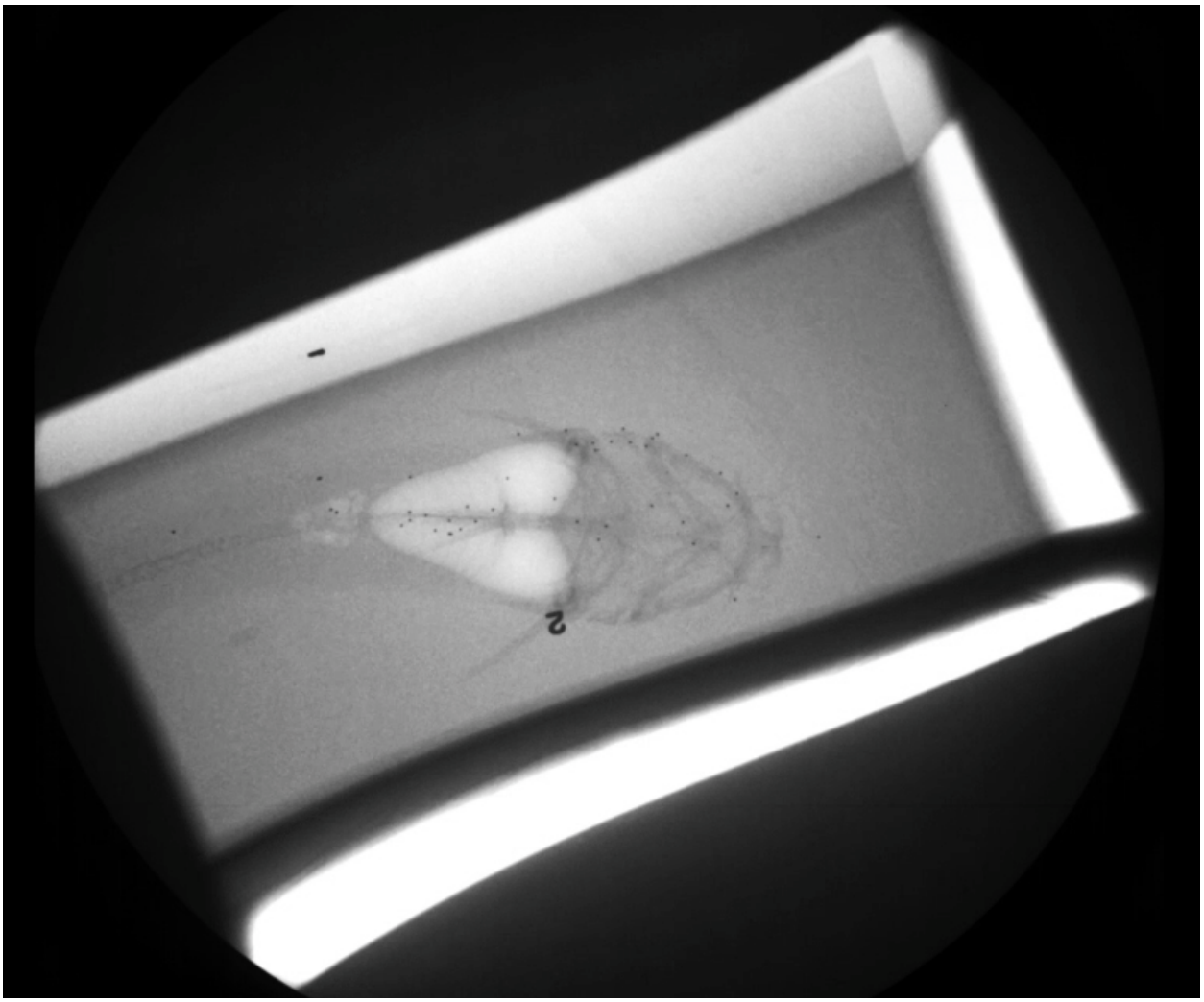

Movie S2. X-ray video of catfish feeding from a dorsoventral view. See supplemental information page for link to video.

Table S4. Ranges of maximum speed and maximum pressure differential in each low and high bin. Number of events in each bin is indicated in parentheses.

	Maximum speed (deg/s)		**Maximum pressure differential (kPa)**	
	Low	***High***	***Low***	***High***
Individual 1 (Cat 01)	13.27-57.3 (30)	57.37-120.59 (31)	0.12-0.75 (30)	0.77-29.97 (31)
Individual 2 (Cat 02)	12.23-48.48 (31)	48.51-345.19 (33)	0.09-0.7 (31)	0.77-26.87 (33)
Individual 3 (Cat 05)	21.25-66.38 (22)	69.88-379.34 (23)	0.15-0.69 (22)	0.69-28.9 (23)

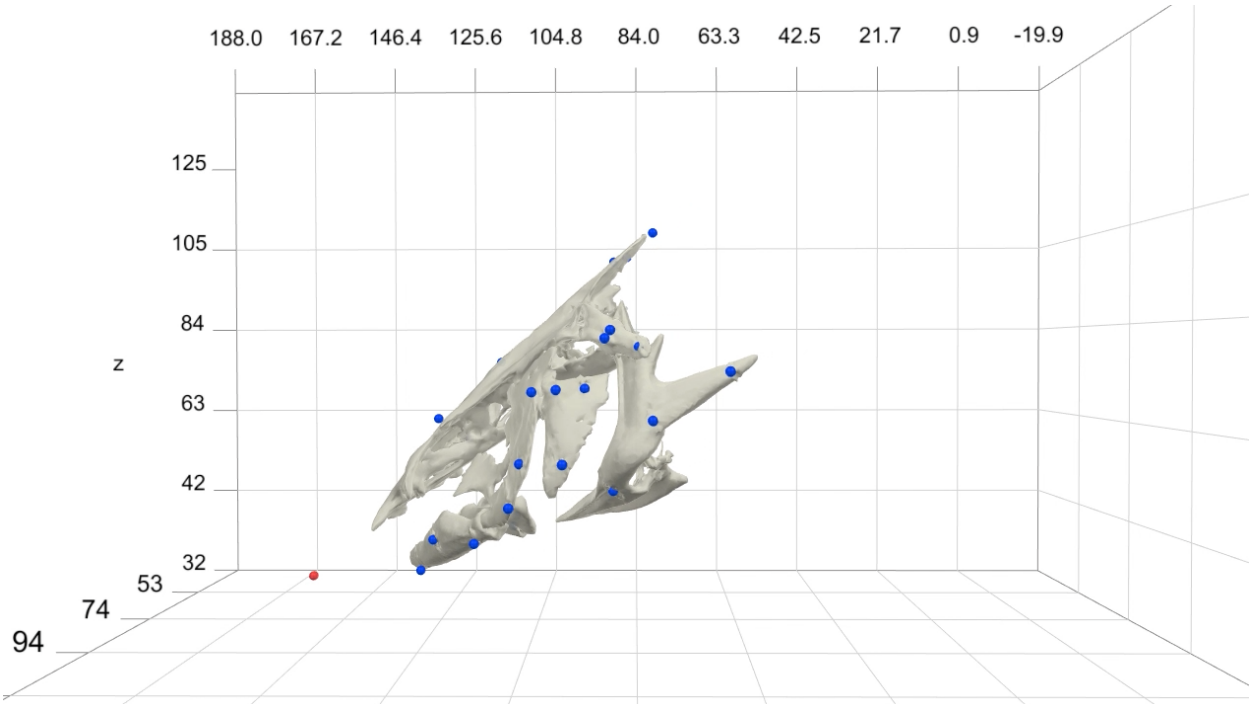

Movie S3. Unification of CT meshes (white) with implanted X-ray markers (blue spheres). The red sphere indicates a marker implanted in the prey item (worm). See supplemental information page for link to video. Video playback is 4x slower than the actual behavior (recorded at 300 frames per second). Video corresponds to trial “Nov 17 2016 Cat 01 Trial 09”.

Table S5. Variability in marker-to-marker distances for each body for each individual (in mm). For each body we measured the distance between each pairwise combination of markers embedded in that element at each frame (e.g. 2 markers would yield a single distance, 2 markers 3 distances, 3 markers 6 distances, etc.). We then measured the standard deviation in these distances for each marker pair over all frames. The statistics in the table below are statistics of those standard deviations: the minimum SD, the max SD, the mean SD, and the SD of the SDs. A higher SD in marker-to-marker distances can indicate deformation or bending of the element (note that muscle distance SDs are higher) or lower reconstruction precision.

Individual 1 (Cat 01), N=15 trials		**Standard deviation of distances for pairwise combinations of markers in each body**			
Body name	**No. markers**	**Min**	**Max**	**Mean**	**SD**
Epaxial	7	0.098	1.717	0.61	0.525
HyoidL	2	0.037	0.037	0.037	NA
Hypaxial	4	1.322	5.056	2.841	1.451
LowerJawL	3	0.06	0.078	0.067	0.01
Neurocranium	6	0.028	0.134	0.087	0.034
OperculumL	3	0.04	0.053	0.047	0.006
PectoralGirdleL	3	0.033	0.066	0.047	0.017
PostTemporalL	3	0.031	0.053	0.041	0.011
Sternohyoid	2	0.193	0.193	0.193	NA
SuspensoriumL	3	0.046	0.083	0.07	0.021
Individual 2 (Cat 02), N=15 trials		**Standard deviation of distances for pairwise combinations of markers in each body**			
Body name	**No. markers**	**Min**	**Max**	**Mean**	**SD**
Epaxial	7	0.049	0.683	0.319	0.207
Hyoid	1	NA	NA	NA	NA
Hypaxial	4	0.725	5.911	3.101	1.841
LowerJawL	4	0.029	0.046	0.035	0.007
Neurocranium	4	0.028	0.081	0.066	0.021
OperculumL	3	0.051	0.212	0.141	0.083
PectoralGirdleL	3	0.034	0.048	0.042	0.007
PostTemporalL	3	0.029	0.108	0.082	0.046
Sternohyoid	2	0.109	0.109	0.109	NA
SuspensoriumL	3	0.033	0.041	0.038	0.004
Individual 3 (Cat 05), N=12 trials		**Standard deviation of distances for pairwise combinations of markers in each body**			
Body name	**No. markers**	**Min**	**Max**	**Mean**	**SD**
Epaxial	7	0.079	1.581	0.713	0.528
HyoidL	3	0.07	0.253	0.191	0.104
Hypaxial	5	0.383	5.699	3.041	1.83
LowerJawL	3	0.082	0.112	0.099	0.015
Neurocranium	4	0.057	0.18	0.102	0.046
OperculumL	3	0.084	0.14	0.113	0.028
PectoralGirdleL	3	0.07	0.165	0.111	0.049
PostTemporalL	3	0.097	0.162	0.12	0.037
Sternohyoid	3	0.294	1.917	1.046	0.818
SuspensoriumL	3	0.054	0.145	0.086	0.051

Movie S4. Light video of Individual 1 (Cat 01) eating pellets (not used for data collection). See supplemental information page for link to video.

Movie S5. Light video of Individual 2 (Cat 02) eating a worm (not used for data collection). See supplemental information page for link to video.

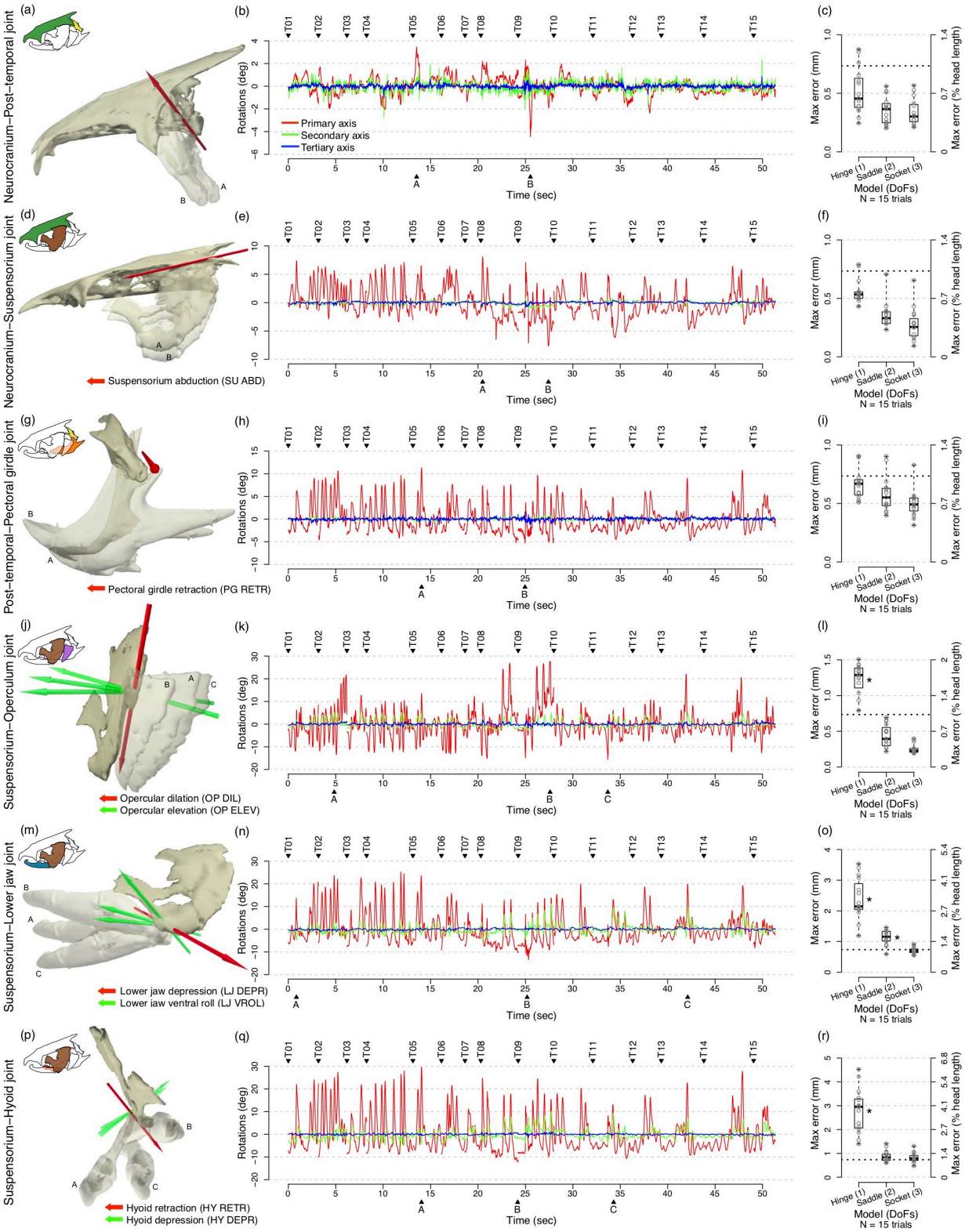

Figure S4. Intracranial joint model fits for Individual 1 (Cat 01). See next page for full caption.

Caption for Figs. S4-S6. The left column (a,d,g,j,m,p) shows the best-fit joint axis or axes for each joint (red: primary/1^o; green: secondary/2^o); only axes with significant rotations are shown. The middle column (b,e,h,k,n,q) shows the rotations about the color-corresponding axis in the left column across all trials from that individual (trials indicated by 'T' labels above the plot). In no case were rotations about the tertiary/3^o axis (blue) considered significant. Axis orientations follow the right-hand rule. Capital letters (A-C) below each plot indicate the corresponding frames at which highlighted positions in the left column were selected. The right column (c,f,i,l,o,r) shows the maximum errors (in mm and as a percent of head length) for all trials for each of the joint models as box plots in black with all values superimposed in grey. A hinge model includes just the 1^o axis, a saddle model axes 1^o and 2^o, and a ball-and-socket model axes 1^o, 2^o, and 3^o. A hinge model has 1 degree of freedom (DoF), a saddle joint has 2 DoFs, and a ball-and-socket model has 3 DoFs. Asterisks denote a mean significantly greater than 1% of head length (black dotted line) by a t-test ($P < 0.01$).

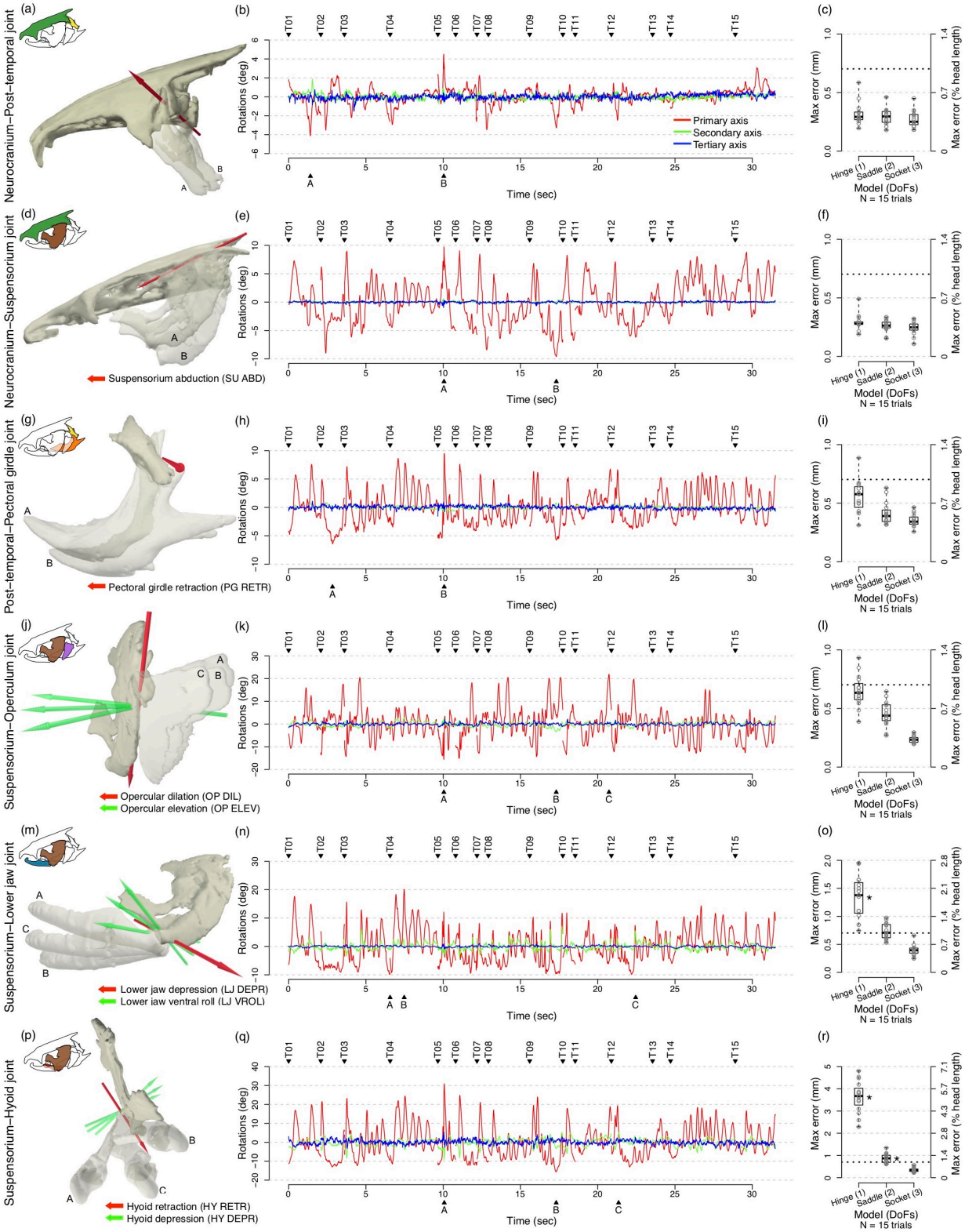

Figure S5. Intracranial joint model fits for Individual 2 (Cat 02). See page following Fig. S4 for full caption.

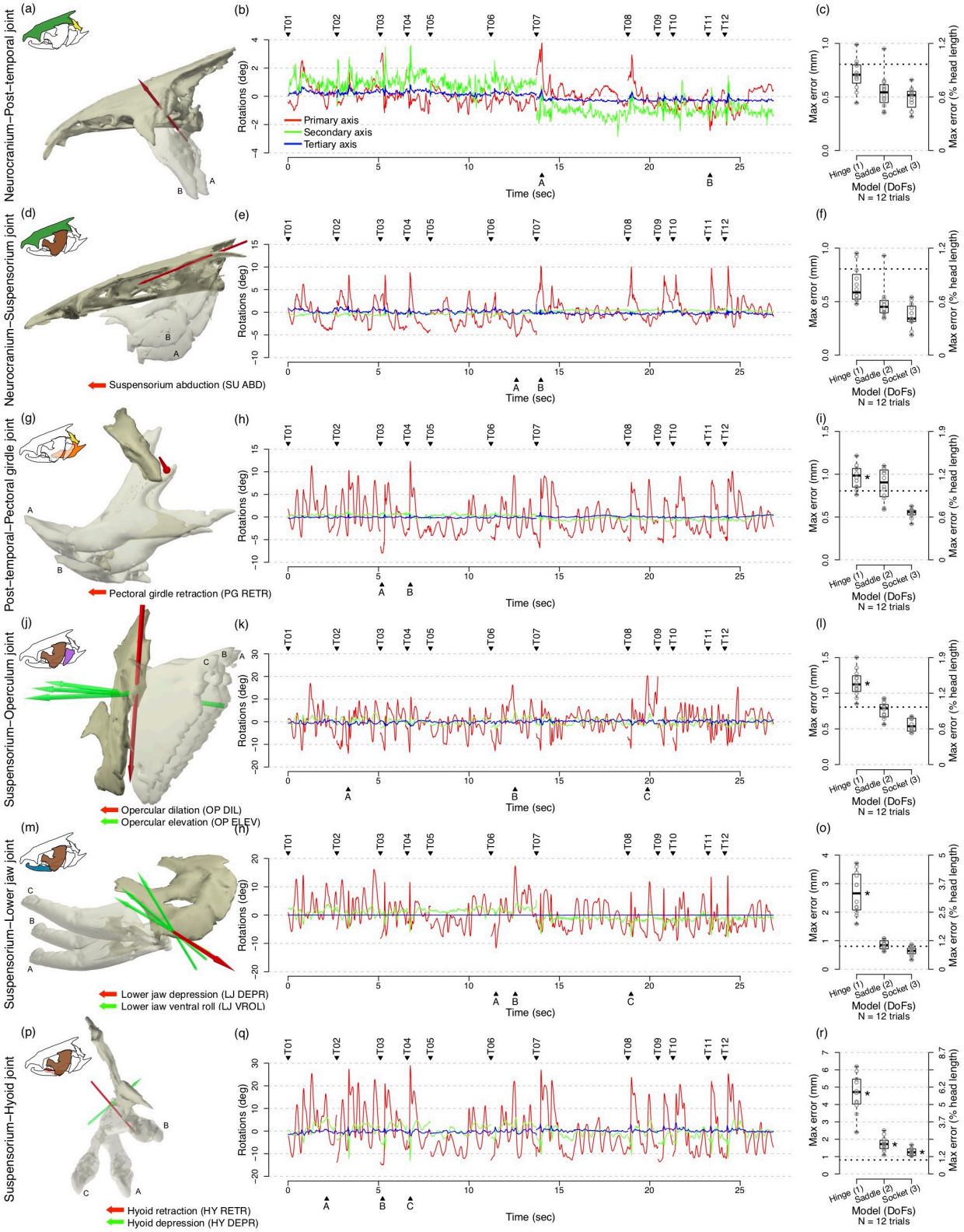

Figure S6. Intracranial joint model fits for Individual 3 (Cat 05). See page following Fig. S4 for full caption.

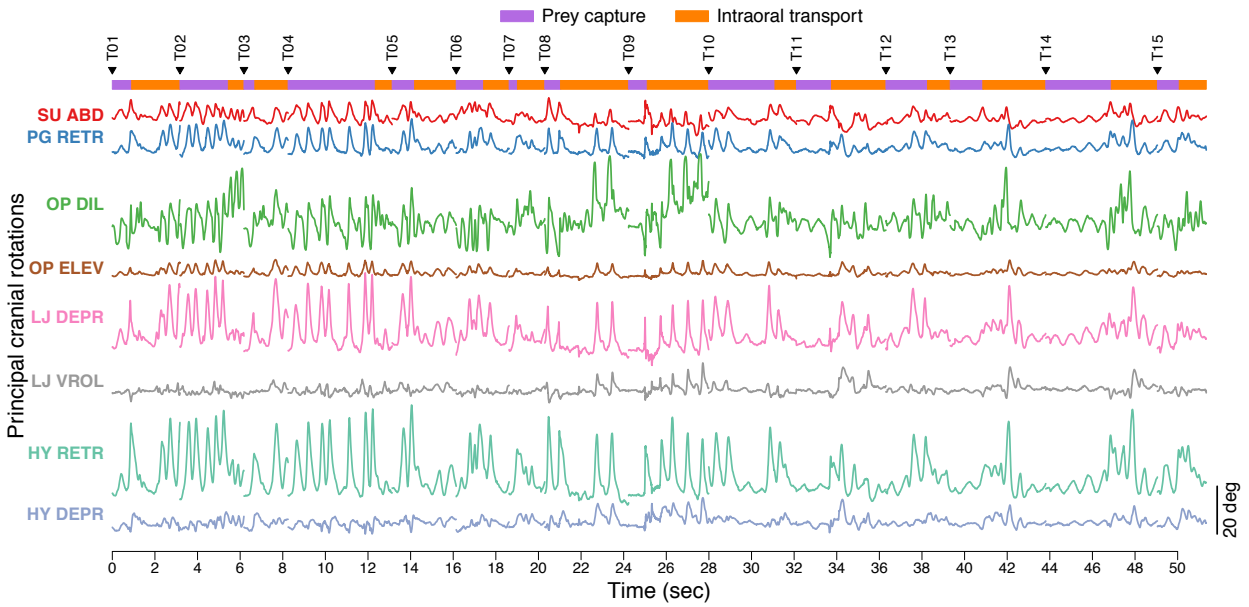

Figure S7. Principal intracranial rotations for individual 1 (Cat 01). See Fig. 3 in manuscript for full caption.

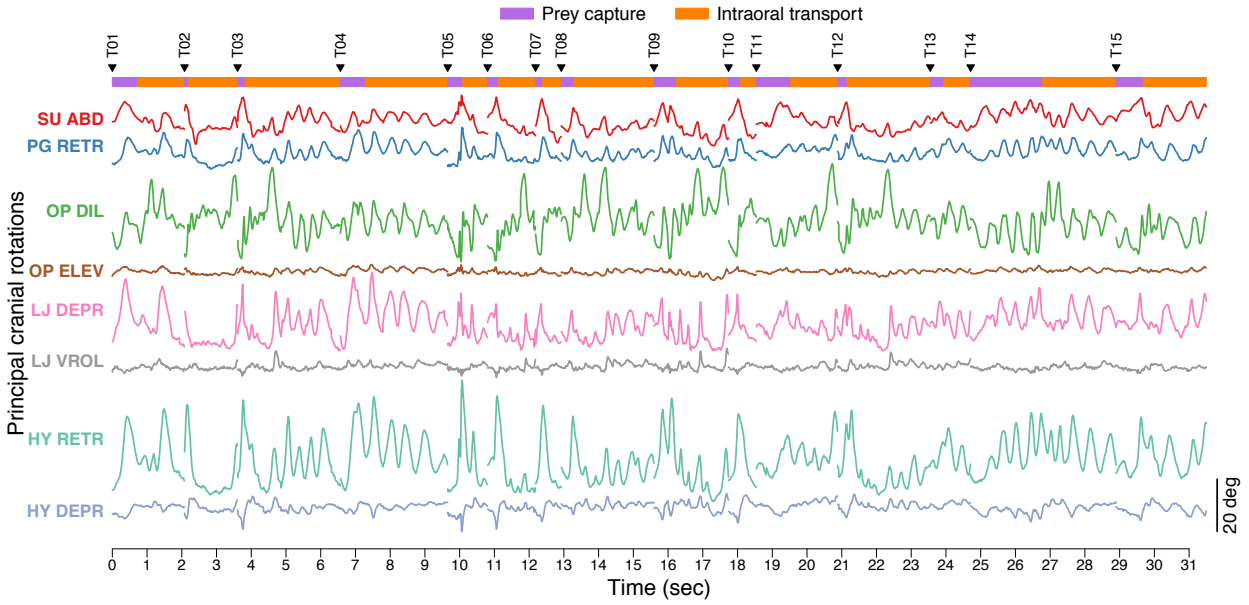

Figure S8. Principal intracranial rotations for individual 2 (Cat 02). Same as Fig. 3 in manuscript (provided here for convenient reference). See Fig. 3 in manuscript for full caption.

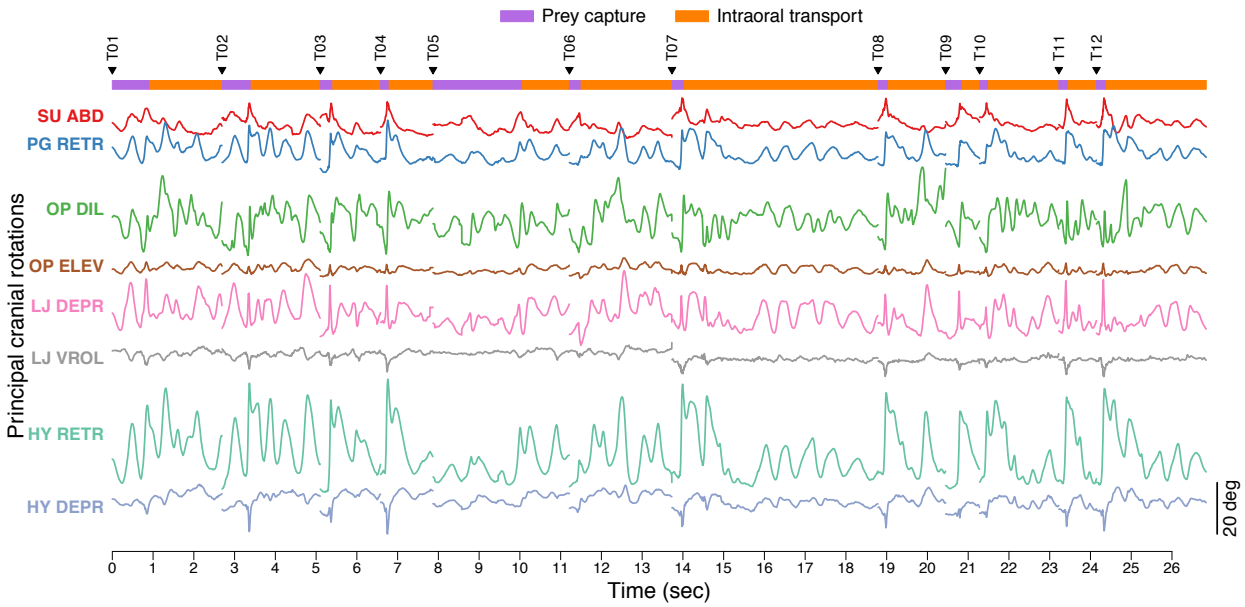

Figure S9. Principal intracranial rotations for individual 3 (Cat 05). See Fig. 3 in manuscript for full caption.

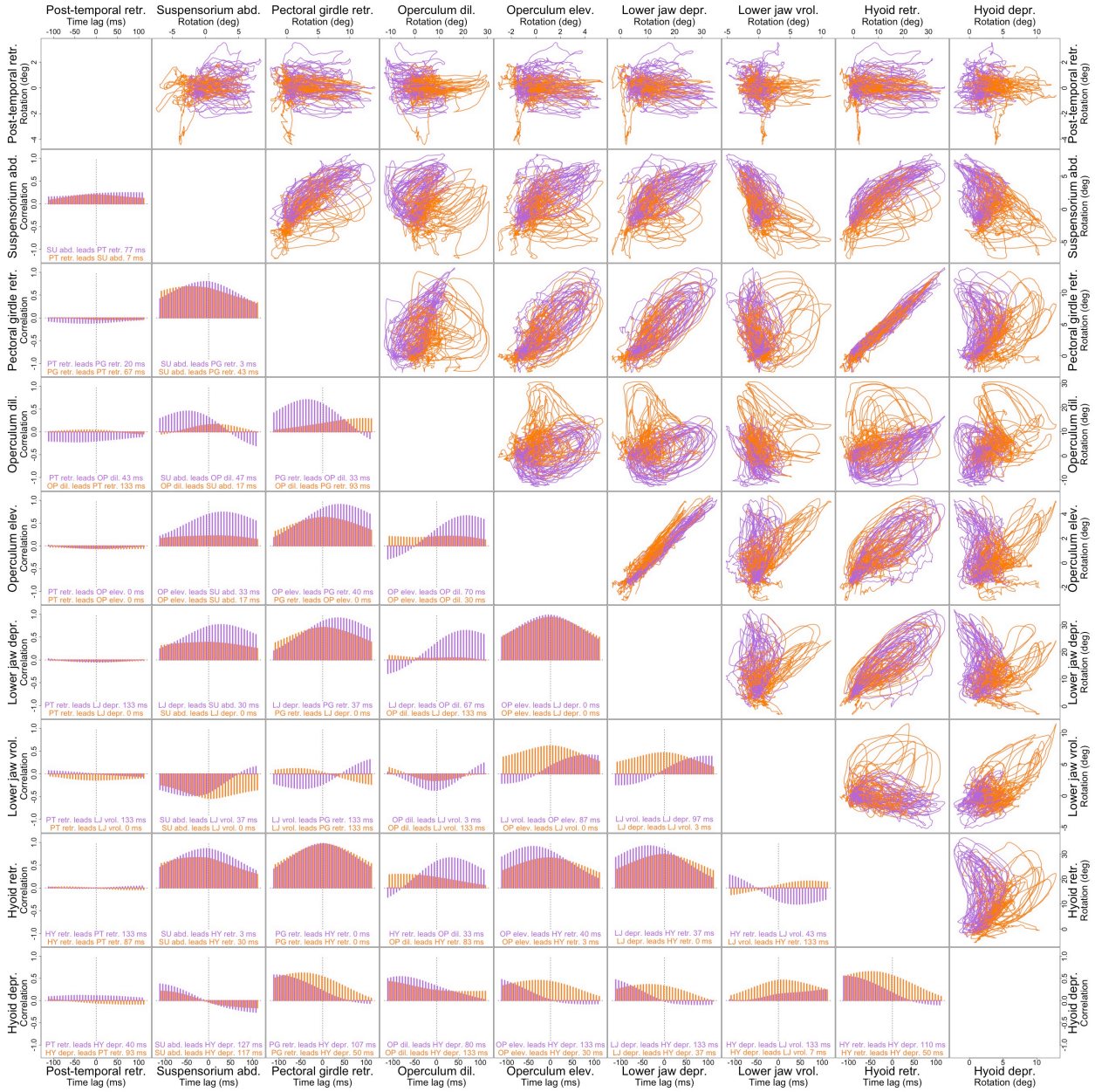

Figure S10. Intracranial motion pairwise plot for Individual 1 (Cat 01). In the upper diagonal are relative motion plots (or angle-angle plots). In the lower diagonal are cross-correlation plots. Purple: prey capture; orange: intraoral transport. To find cross-correlation values we took the maximum absolute value over the range of lags indicated.

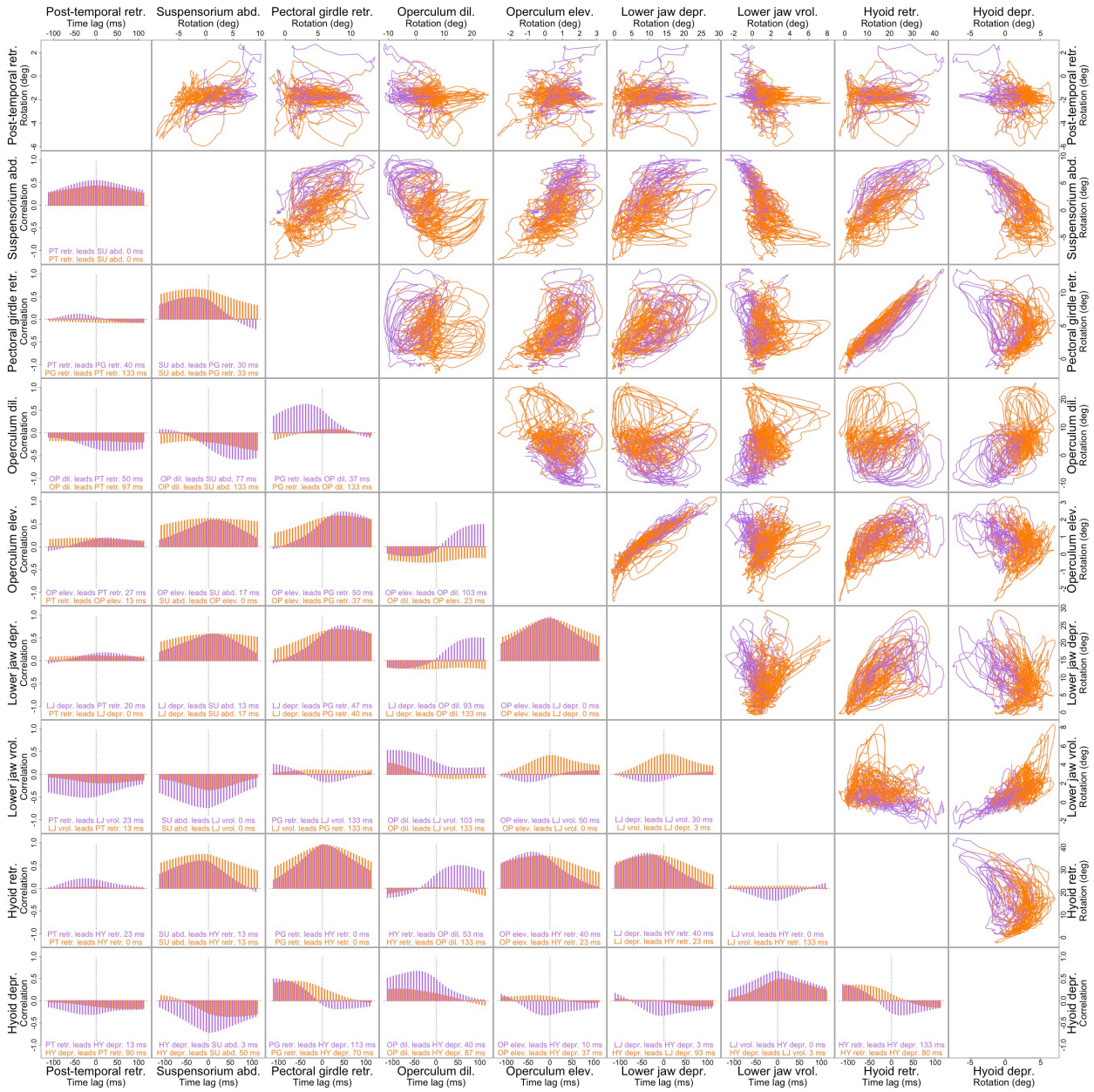

Figure S11. Intracranial motion pairwise plot for Individual 2 (Cat 02). In the upper diagonal are relative motion plots (or angle-angle plots). In the lower diagonal are cross-correlation plots. Purple: prey capture; orange: intraoral transport. To find cross-correlation values we took the maximum absolute value over the range of lags indicated.

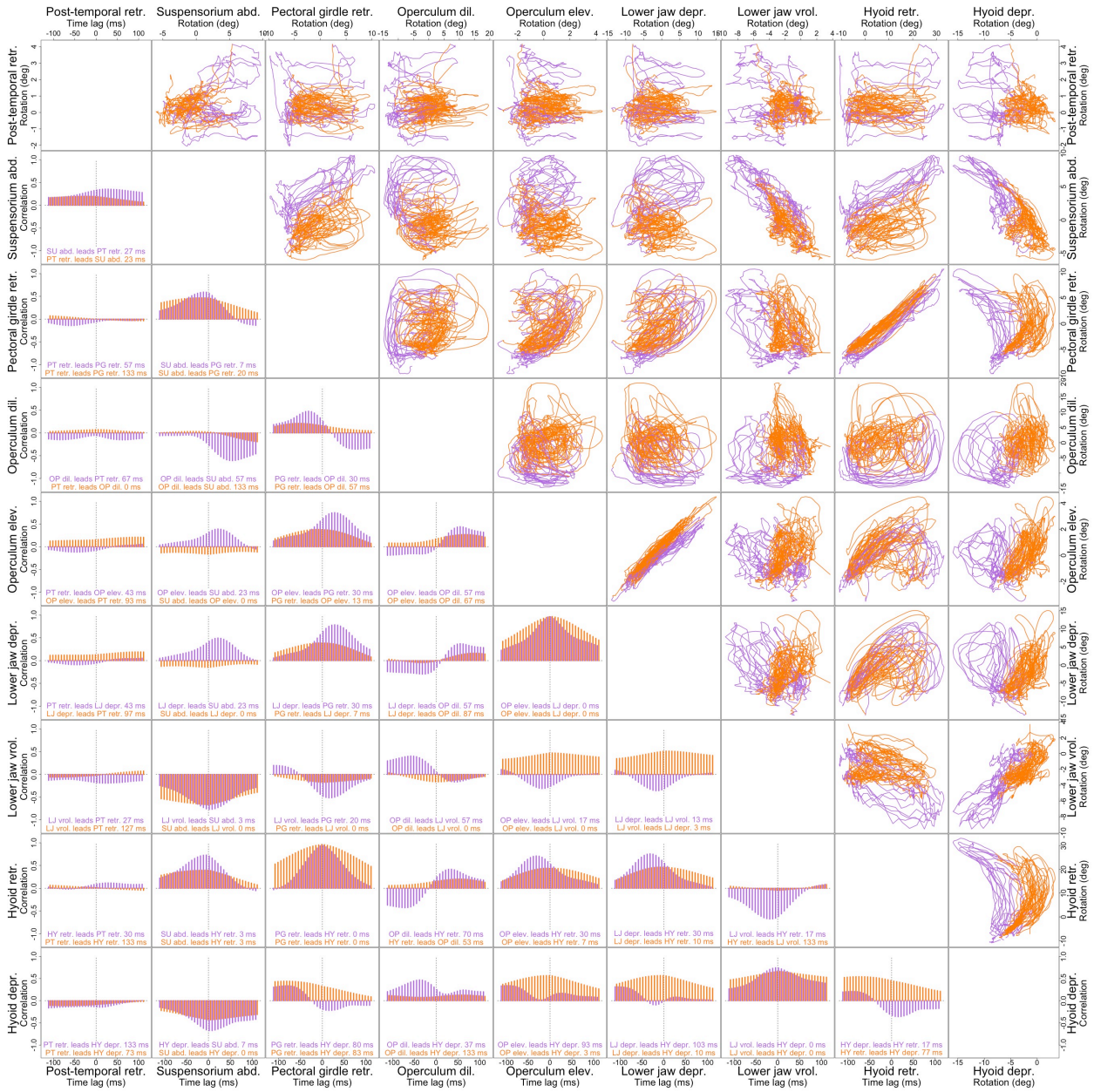

Figure S12. Intracranial motion pairwise plot for Individual 3 (Cat 05). In the upper diagonal are relative motion plots (or angle-angle plots). In the lower diagonal are cross-correlation plots. Purple: prey capture; orange: intraoral transport. To find cross-correlation values we took the maximum absolute value over the range of lags indicated.

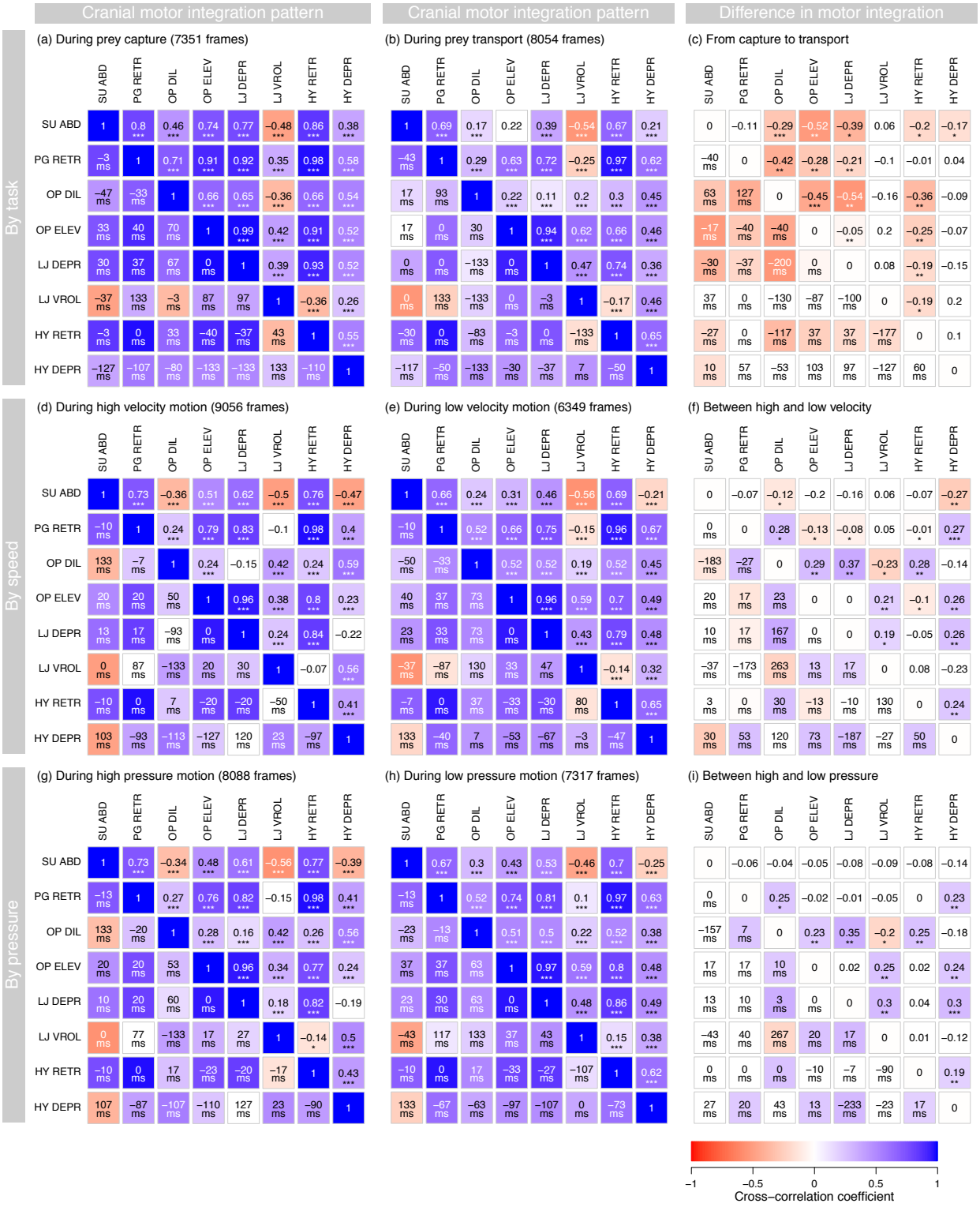

Figure S13. Cranial motor integration patterns for Individual 1 (Cat 01). Similar to Fig. 4 but with motor integration patterns also grouped by speed and intraoral pressure.

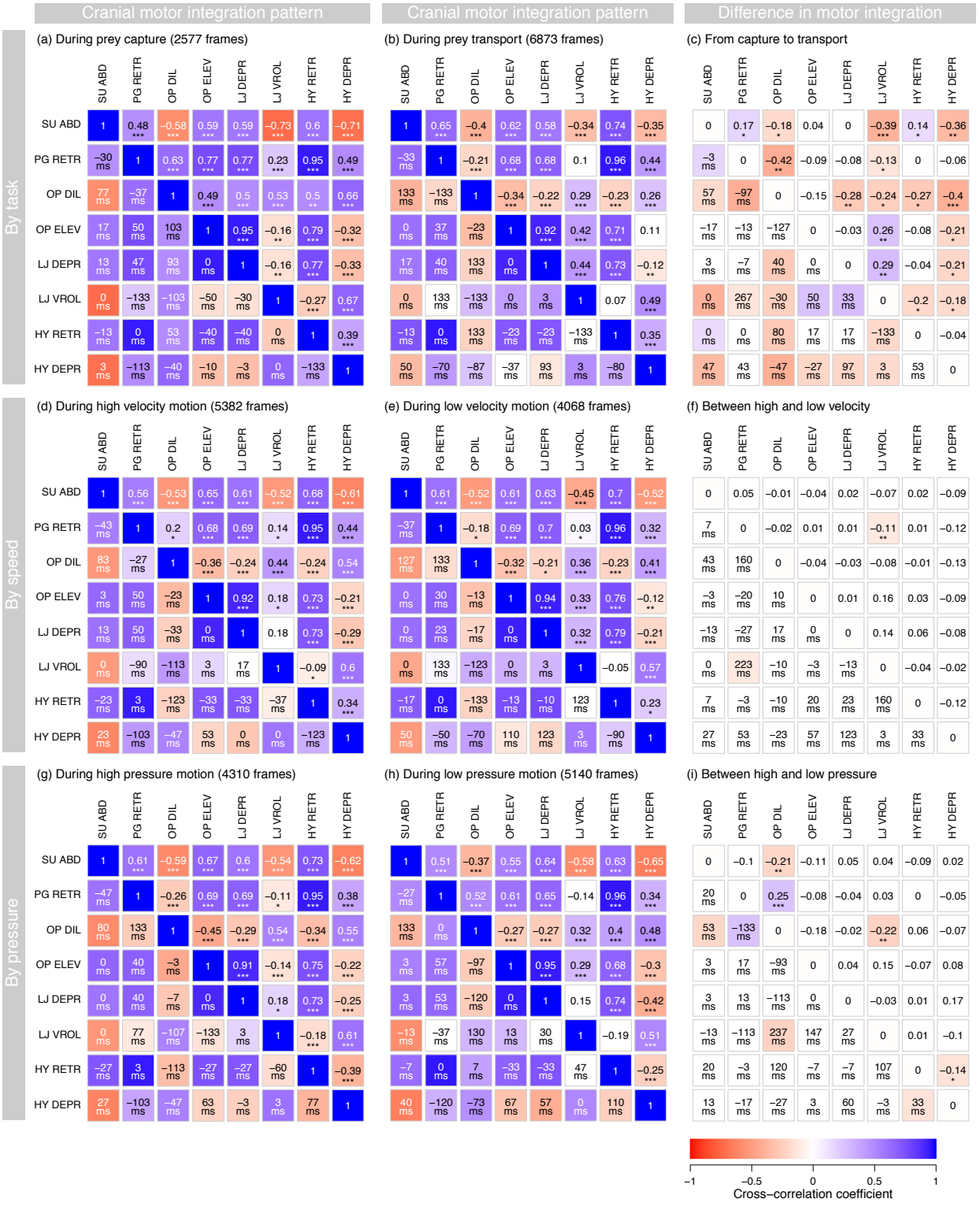

Figure S14. Cranial motor integration patterns for Individual 2 (Cat 02). Same as Fig. 4 but with motor integration patterns also grouped by speed and intraoral pressure differential.

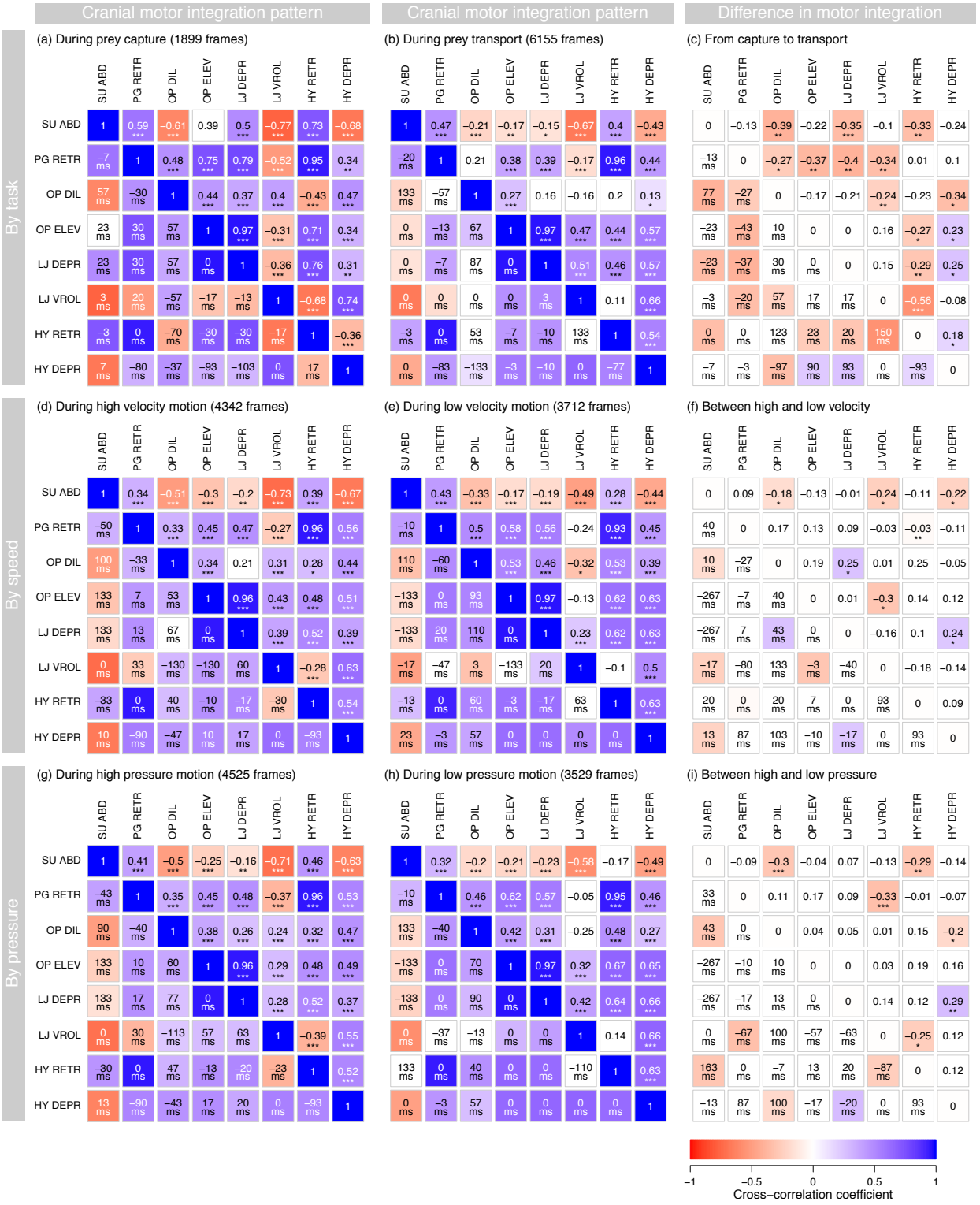

Figure S15. Cranial motor integration patterns for Individual 3 (Cat 05). Similar to Fig. 4 but with motor integration patterns also grouped by speed and intraoral pressure differential.

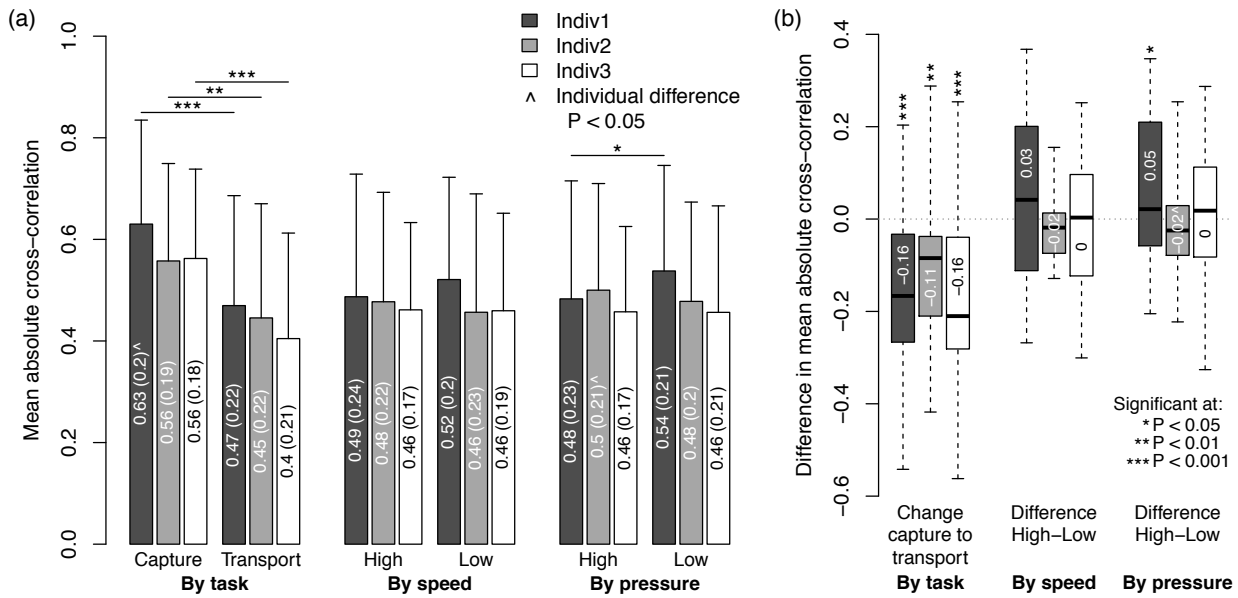

Figure S16. Mean motion integration differences by task, speed, and pressure differential for all individuals. Mean intracranial motion integration was significantly greater ($P < 0.01$, asterisks) during capture than during transport for all individuals (a-b, left). In contrast, no strong and consistent significant differences in mean integration were found between mouth open-close events grouped by magnitude of speed (a-b, middle) or intraoral pressure differential (a-b, right). Some significant individual differences were identified ($P < 0.05$, carets) but not in the mean integration differences between capture and transport (b, left). Values within bars are mean (SD) in (a) and mean in (b). Significance statistics were determined by randomization tests.

Motion integration (cross-correlation) during prey capture				
Skeletal element pair	**Individual 1**	**Individual 2**	**Individual 3**	**Mean**
Lower_jaw-Hyoid	0.51	0.51	0.62	0.55
Operculum-Hyoid	0.66	0.57	0.49	0.57
Operculum-Lower_jaw	0.60	0.54	0.51	0.55
Pectoral_girdle-Hyoid	0.78	0.72	0.64	0.71
Pectoral_girdle-Lower_jaw	0.64	0.50	0.65	0.60
Pectoral_girdle-Operculum	0.81	0.70	0.61	0.71
Suspensorium-Hyoid	0.62	0.66	0.70	0.66
Suspensorium-Lower_jaw	0.63	0.66	0.63	0.64
Suspensorium-Operculum	0.60	0.58	0.50	0.56
Suspensorium-Pectoral_girdle	0.80	0.48	0.59	0.62
Motion integration during prey transport				
Skeletal element pair	**Individual 1**	**Individual 2**	**Individual 3**	**Mean**
Lower_jaw-Hyoid	0.43	0.35	0.45	0.41
Operculum-Hyoid	0.47	0.33	0.34	0.38
Operculum-Lower_jaw	0.46	0.46	0.44	0.46
Pectoral_girdle-Hyoid	0.79	0.70	0.70	0.73
Pectoral_girdle-Lower_jaw	0.48	0.39	0.28	0.39
Pectoral_girdle-Operculum	0.46	0.44	0.30	0.40
Suspensorium-Hyoid	0.44	0.55	0.42	0.47
Suspensorium-Lower_jaw	0.46	0.46	0.41	0.45
Suspensorium-Operculum	0.19	0.51	0.19	0.30
Suspensorium-Pectoral_girdle	0.69	0.65	0.47	0.60
Change in motion integration from capture to transport				
Skeletal element pair	**Individual 1**	**Individual 2**	**Individual 3**	**Mean**
Lower_jaw-Hyoid	-0.08	-0.16	-0.17	-0.14
Operculum-Hyoid	-0.19	-0.24	-0.15	-0.20
Operculum-Lower_jaw	-0.14	-0.07	-0.07	-0.09
Pectoral_girdle-Hyoid	0.02	-0.03	0.06	0.02
Pectoral_girdle-Lower_jaw	-0.15	-0.11	-0.37	-0.21
Pectoral_girdle-Operculum	-0.35	-0.25	-0.32	-0.31
Suspensorium-Hyoid	-0.18	-0.11	-0.29	-0.19
Suspensorium-Lower_jaw	-0.16	-0.20	-0.22	-0.19
Suspensorium-Operculum	-0.41	-0.07	-0.31	-0.26
Suspensorium-Pectoral_girdle	-0.11	0.17	-0.13	-0.02

Table S5. Table of motion integration between each pair of skeletal elements during feeding (from which Fig. 6 in the main text is drawn). Integration is grouped by capture (top), feeding (middle), and the difference between capture and feeding (bottom). Values for each element pair are the mean of all cross-correlations that include that element for that individual. In the case where the motion of both elements is described by a single axis (Suspensorium-Pectoral girdle is the only case) this is simply the cross-correlation between rotations about those two axes. For all other cases these values are the means of multiple cross-correlations (e.g. Suspensorium-Operculum would be the mean of suspensorium abduction-opercular dilation and suspensorium abduction-opercular elevation). Element pairs for which motion integration changes by more than the average across all pairs (0.14) are indicated in blue in the bottom section.